Aerospace Science and Technology 106 (2020) 106210

Contents lists available at ScienceDirect

Aerospace Science and Technology

www.elsevier.com/locate/aescte

Design and analysis of non-axisymmetric installed aero-engine exhaust systems

John J. Otter *, Ioannis Goulos, Robert Christie, David G. MacManus

Centre for Propulsion Engineering, School of Aerospace, Transport and Manufacturing, Cranfield University, Bedfordshire, MK43 0AL, United Kingdom of Great Britain and Northern Ireland

ARTICLE INFO

Article history:
Received 10 June 2020
Received in revised form 9 September 2020
Accepted 12 September 2020
Available online 17 September 2020
Communicated by Cummings Russell

Keywords:
Aero-engine
Computational Fluid Dynamics
Exhaust Nozzle
Class Shape Transformation
Propulsion System Integration
Engine-airframe Integration

ABSTRACT

In order to increase propulsive efficiency, and hence reduce fuel consumption, future aero-engines are expected to operate with higher bypass ratios and larger fan diameters relative to current in-service engines. As such, propulsion systems are likely to be more closely-coupled with the airframe which is expected to accentuate detrimental aerodynamic interference effects between the engine and airframe. It is therefore crucial that the design of future aero-engine exhaust systems is considered as part of an engine-airframe configuration in order to ensure that the expected benefits of high BPR engines are realised. This work presents the aerodynamic performance and evaluation of a set of novel exhaust systems within complete engine-airframe configurations. The introduction of non-axisymmetric exhaust systems was shown to mitigate the aerodynamic penalties associated with closely-coupled propulsion systems at cruise conditions. Relative to an axisymmetric baseline configuration, the introduction of non-axisymmetric bypass and core nozzles were found to increase the net vehicle force of the engine-airframe configuration by 0.8% and 0.6% respectively. As a result of this work, it can be concluded that non-axisymmetric exhaust systems represent a viable method for reducing aircraft cruise fuel burn.

1. Introduction

1.1. Background

In order to increase propulsive efficiency, and hence reduce fuel consumption, future aero-engines are expected to operate with higher bypass ratios [1,2], lower fan pressure ratios [3] and larger fan diameters relative to current in-service engines. As a result, the overall efficiency of future aero-engines will become more dependent upon the aerodynamic performance of the exhaust system [4]. Moreover, due to larger fan diameters, future civil aircraft are likely to feature propulsion systems which are more closely-coupled with the airframe. For a podded underwing configuration, this is expected to accentuate detrimental aerodynamic interference effects between the engine and airframe [5–7]. It is therefore crucial that the design of future aero-engine exhaust systems is considered as part of an engine-airframe configuration in order to ensure that the expected benefits of high bypass ratio (BPR) engines are realised.

1.2. Aero-engine exhaust system design

An aero-engine exhaust system serves two main functions: to generate propulsive thrust with as little total pressure loss at possible [8] and to match the flow capacity requirements from the fan and lower pressure turbine [9]. The design of axisymmetric exhaust systems in an engine-only configuration has been the subject of recent research and robust design methods for such configurations have been established [4,10–14]. However, in practice aero-engine exhaust geometries are not axisymmetric but feature circumferential geometry variations for a number of reasons. Such geometry variations may be required to facilitate the integration of structural bifurcations and other engine mounting systems. In addition, the introduction of non-axisymmetric exhaust systems has been highlighted as a means of reducing jet noise [15–17]. As aerodynamic interaction between the airframe wing and engine exhaust system leads to circumferential pressure field variation on the exhaust afterbodies [18], there is potential for the exhaust afterbodies to be redesigned to account for any loss due to this variation. To this end, Otter et al. [19] developed a method for developing non-axisymmetric bypass nozzles. With this method it was demonstrated that non-axisymmetric engine-only configurations operating at representative cruise conditions could increase

* Corresponding author.
E-mail address: jjotter26@gmail.com (J.J. Otter).

https://doi.org/10.1016/j.ast.2020.106210

Nomenclature

Roman symbols

dS	Infinitesimal surface element normal to surface	m^2
dA	Infinitesimal surface element parallel to surface	m^2
V	Velocity vector	$m\,s^{-1}$
$\dot{m}$	Mass flow rate	$kg\,s^{-1}$
C_{V*}	Modified velocity coefficient	–
F_G	Gauge Stream Force	N
GPF_{*c}	Corrected modified gross propulsive force	N
l_{cc}	Core cowl length	m
NPF	Net propulsive force	N
NPF_c	Corrected net propulsive force	N
NVF	Net vehicle force	N
p	Static Pressure	Pa
p_0	Total Pressure	Pa
$r^{in}_{BP-exit}$	Bypass nozzle exit inner radius	m
$r^{in}_{CR-exit}$	Core nozzle exit inner radius	m
$r^{out}_{BP-exit}$	Bypass nozzle exit outer radius	m
$r^{out}_{CR-exit}$	Core nozzle exit outer radius	m
r^{te}_{plug}	Core nozzle plug radius	m

Greek symbols

α	Airframe angle of attack	degrees
β_{cc}	Core cowl angle	degrees
ϕ	Force in the drag domain	N
ψ	Azimuthal angle	degrees
ρ	Density	$kg\,m^{-3}$
τ	Local shear stress	Nm^{-2}
θ	Force in the thrust domain	N

Superscripts and subscripts

^{D}	Force resolved in drag direction
^{L}	Force resolved in lift direction

Acronyms

BPR	Bypass Ratio
CRM	Common Research Model
DOE	Design of Experiments
DSFRN	Dual Separate Flow Reference Nozzle
GCI	Grid Convergence Index
iCST	intuitive Class Shape Transformation

engine net propulsive force by 0.12% relative to an axisymmetric case [19]. However, the impact of non-axisymmetric exhaust systems on engine-airframe interaction has yet to be assessed in the open literature.

1.3. Aerodynamic aspects of propulsion system integration

Engine-airframe integration is a multi-disciplinary topic with both mechanical and aerodynamic requirements [20]. In terms of underwing installation, the axial and vertical location of the engine relative to the wing leading edge are key design variables [5]. Mechanical design constraints such as engine ground clearance, pylon structural requirements, wing flutter speed and wing flutter frequency are known to be functions of engine installation position [20]. Given the expected increase of engine fan diameters, it is likely that the vertical offset between the wing leading edge and engine will be reduced in order to maintain ground clearance requirements. Furthermore, engines could be potentially positioned axially coincident or overlapping with the wing leading edge in order to minimise the bending moment that will arise due to increased engine weight. Installation in such closely-coupled positions has been shown to be detrimental to the aerodynamic performance of the combined engine-airframe system [21,6]. For example, an aerodynamic assessment by Sibilli et al. [6] demonstrated that an engine installed aft of the wing leading edge had a 2.5% larger fuel burn compared to the case with the engine installed with the same axial offset forward of the wing leading edge. As such, the installation of the next generation of turbofan engines may require compromises to be made to the aerodynamic performance of the engine-airframe system in order to create a balanced engine installation.

Although research into aerodynamic aspects of propulsion system integration [21,6,5,18,22] and the aerodynamic optimisation of aero-engines as engine-only configurations [23–26,10–12] is well established, there is a lack of literature which addresses how aero-engine nacelles and exhaust nozzles should be designed in order to maximise the aerodynamic performance of a combined system. The few engine-airframe studies which consider the design of the engine or airframe geometry in an aircraft configuration are often limited by model assumptions. For example, the use of full potential flow solvers [27,20], the use of through flow nacelles [28–31] or by neglecting the engine pylon [31]. Although the work of Lei et al. [32] models a separate-jet engine with a pylon, the study is for lower BPR of 8. Therefore, there is a requirement to investigate how nacelle and exhaust nozzles for Ultra-High BPR engines should be designed as part of a combined engine-airframe configuration.

1.4. Scope of present work

The increased sensitivity of specific fuel consumption to exhaust system performance, combined with closely-coupled installation positions, means that it is essential to analyse the integrated engine-airframe system as a whole. Hence, in order to obtain the proposed fuel burn reductions of high BPR engines, it is vital that further research be conducted into the effects of engine-airframe integration on both the exhaust and airframe system performance. Therefore the aim of the research is to assess how design changes to the engine exhaust system affect the aerodynamic performance of the complete engine-airframe system. Therefore, two research objectives have been outlined. Firstly, to quantify the effect of exhaust system design changes on the aerodynamic performance of the full airframe-engine system. Secondly, to explore the design space of novel exhaust systems geometries as part of an engine-airframe configuration.

To the authors' knowledge no computational study to date has assessed the influence of exhaust system design on the aerodynamic performance of an engine-airframe configuration. This paper presents a contribution to knowledge through a unique design space exploration of underwing separate-jet exhaust systems. Furthermore, the benefits of a non-axisymmetric exhaust system can only be assessed through the analysis of a combined engine-airframe system and therefore this study represents a change in design philosophy away from designing engine exhausts in isolation.

2. Methodology

2.1. Thrust and drag accounting

The thrust and drag bookkeeping method and engine station numbering system are based upon an established method [33]

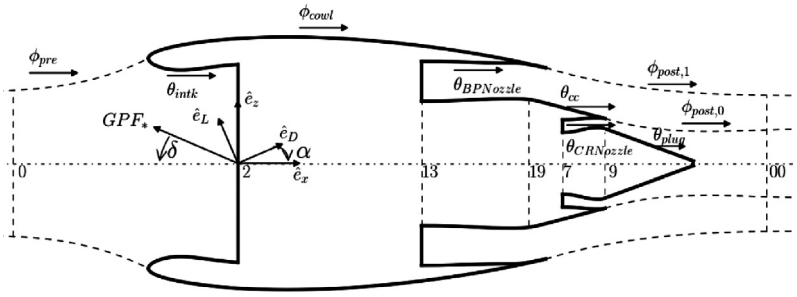

(a) Forces acting on isolated Aero-engine [18]

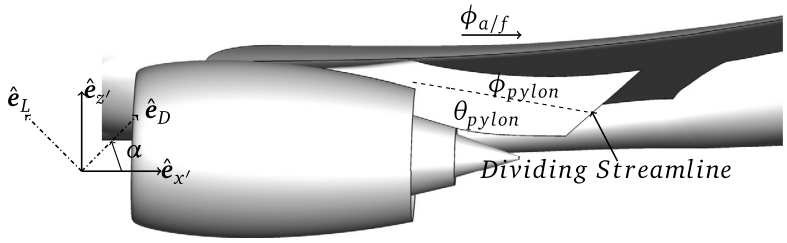

(b) Installed thrust and drag bookkeeping schematic with the thrust pylon split shown.

Fig. 1. Thrust and Drag Accounting System.

which has been reported in other publications [5,18,19]. Furthermore, the correction method for net propulsive force of Otter et al. [18,19] was used in order to account for any differences between the intake and nozzle mass flows due to engine integration. However, the aforementioned methods do not account for the engine pylon which connects the engine and airframe. As a result an extension to the method is outlined in order to account for such a pylon. The force which acts on the pylon was split into two parts: θ_{pylon}, which is accounted for in the engine net propulsive force (NPF), and ϕ_{pylon} which is accounted for in the aircraft drag domain (Fig. 1b). The thrust part of the pylon was defined as the section of the pylon which the bypass jet washes over. This split was undertaken numerically based on the total temperature on the pylon surface due to the difference in total temperature between the freestream and bypass jet.

The modified thrust coefficient (C_{V*}) [18,19], resolved into the drag and lift directions is given by Eqs. (1) and (2) where ϕ^D, θ^D denote wall forces, F_G^D denotes a gauge stream force (Eqs. (3) and (4) from [18,19]). Note that the subscript D denotes a force which has been resolved into the drag axis aligned with the freestream flow and the subscript L denotes a force resolved into the lift axis (normal to the freestream flow). The corrected gross propulsive force (GPF_{*c}) and corrected net propulsive force (NPF_{*c}) can be calculated according to the method outlined by Otter et al. [18,19].

$$C_{V*}^D = \frac{F_{G19}^D + F_{G9}^D + \theta_{cc}^D + \theta_{plug}^D + \theta_{pylon}^D}{\dot{m}_7 V_7^{ideal} + \dot{m}_{13} V_{13}^{ideal}} \tag{1}$$

$$C_{V*}^L = \frac{F_{G19}^L + F_{G9}^L + \theta_{cc}^L + \theta_{plug}^L + \theta_{pylon}^L}{\dot{m}_7 V_7^{ideal} + \dot{m}_{13} V_{13}^{ideal}} \tag{2}$$

$$\phi^D, \theta^D = \iint_{surface} ((p - p_{atm})\hat{\mathbf{e}}_D \cdot \mathbf{dS} + \iint_{surface} \tau \hat{\mathbf{e}}_D \cdot \mathbf{dA} \tag{3}$$

$$F_G^D = \iint_{Area} (\rho |\mathbf{V}| \mathbf{V} \cdot \hat{\mathbf{e}}_x + (p - p_{atm}))\mathbf{dS} \cdot \hat{\mathbf{e}}_D \tag{4}$$

To quantify the overall performance of the combined engine-airframe system, a net vehicle force (NVF^D, Eq. (5)) is defined as the difference between the corrected engine net propulsive force and the airframe drag [5]. At cruise conditions the net vehicle force of the engine-airframe system should be zero such that steady flight is obtained. However, due to the fixed engine operating conditions considered within this work, there is a small resultant force on the engine-airframe system. Hence, the absolute value of the net vehicle force is not of primary interest, but a comparison between configurations was achieved through comparing changes in the net vehicle force. Throughout this work the net vehicle force is reported as a percentage change relative to a baseline case normalised by the clean airframe drag (denoted ΔNVF^D) and hence a ΔNVF^D value of 1% equates to 2.3 drag counts.

$$NVF^D = NPF_c^D - \phi_{a/f}^D - \phi_{pylon}^D \tag{5}$$

$$\phi_{total}^L = NPF_c^L + \phi_{a/f}^L + \phi_{pylon}^L \tag{6}$$

2.2. Engine cycle and airframe

This airframe used in the study is based on the previous installation studies by Otter et al. [18]. The airframe geometry was the NASA wing/body/horizontal-tail Common Research Model (CRM) airframe geometry from the fourth Drag Prediction Workshop [34]. The operating condition for the airframe in this study corresponds to an altitude of 35,000 ft, a Mach number of 0.85 and a lift coefficient of 0.5.

The engines are based upon the future high BPR turbofan architecture that was investigated by Otter et al. [19]. The configurations were designed to have a BPR above 15, to cruise at a freestream Mach number of 0.85 with a rated cruise standard net thrust of approximately 60 kN (based on the cruise drag of the CRM airframe) [19]. The bypass nozzle operated with a pressure ratio of 2.2 and the core nozzle with a pressure ratio of 1.6 [19]. Within this study one operating condition was considered in order to quantify the performance of non-axisymmetric

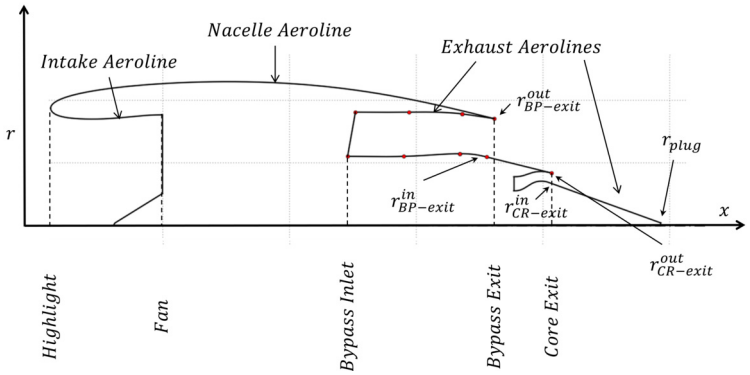

Fig. 2. Aerolines in the x-r plane [19].

exhaust systems at a representative mid-cruise condition. Although the performance across the cruise segment as well as at off-design conditions is also of importance for the aircraft system, it was considered to be out of scope for this present study and a useful direction for future research.

The underwing installation of the engine remained fixed for all of the investigated configurations. The axial position of the nacelle topline trailing edge was set to be coincident with the airframe leading edge with a vertical offset equal to 9% of the local wing chord between the wing leading edge and nacelle trailing edge. This is therefore representative of a closely-coupled installation position.

2.3. Geometry generation

The non-axisymmetric separate-jet nozzles were designed with the method outlined by Otter et al. [19]. With this method three-dimensional non-axisymmetric aero-engine geometries are constructed by defining multiple aerolines around an azimuth in a cylindrical co-ordinate system [19]. An example set of aerolines in the x-r plane is shown in Fig. 2. The method is fully parametric and utilises intuitive Class Shape Transformation functions (iCST) [35]. Within this study two types of exhaust system design are investigated: bypass nozzle with circumferential variation of the nacelle exit radius (Section 3.2.1) and non-concentric bypass nozzles (Section 3.2.2).

2.3.1. Pylon design

Although the CRM geometry features a pylon, it is not suitable for separate-jet exhausts or for the engine position considered in this study. Therefore a pylon design methodology was developed in order to create an aerodynamically feasible design. The engine pylon was constructed by stacking aerofoils in the vertical direction (parallel to the radial co-ordinate of the engine an azimuthal angle of 0). Aerofoils were defined with iCSTs with the five parameter approach of Kulfan [36,37]. In addition, iCSTs were also used to control the variation of each aerofoil parameter. Therefore, non-linear variation of the leading edge could be prescribed, as opposed to a simple aerofoil sweep. The thrust and drag portions of the pylon were constructed as one shape. From this shape the engine geometry was then subtracted through a boolean operation. The heat shield line was defined as an iCST with a start point at the trailing edge of the core cowl and an end point at the trailing edge of the pylon. After the definition of the heat shield line the portion of the pylon which lies in the core duct was then removed via a boolean subtraction.

The pylon geometries used within this study were obtained through a number of design iterations to remove shock-induced separation which formed on the inboard side of the pylon forebody. The base pylon design was the same for each engine configuration. However, each engine configuration had a bespoke heat-shield design due to the variation in core cowl design. As the scope of this study is on centred on exhaust system design, the effect of pylon modifications on overall aircraft performance were not considered but could offer additional benefits [38].

2.4. Computational approach

The computational approach used within this study has been reported by Otter et al. [19,18,14] and as such only a brief summary is given here. An implicit density based compressible solver with a second order upwind spatial scheme [39] was used to solve the Reynolds-averaged Navier-Stokes equations. The $k-\omega$ Shear Stress Transport turbulence model [40] was used to close the RANS equations based on the outcome of the validation studies for both the aircraft and isolated separate jet configurations [41,14].

The computational domain consisted of a hemispherical fluid domain with a pressure far-field boundary condition used to model the freestream conditions, Fig. 3a. The diameter of this hemispherical domain was chosen to be 100c in accordance with the recommendations from the fourth drag prediction workshop [42]. The freestream Mach number, atmospheric static pressure (p_0) and airframe angle of attack (α) were applied along this hemispherical boundary. The engine fan face was modelled as a pressure outlet boundary condition, Fig. 3a, with a target mass flow set according to the required operating point. Pressure inlet boundary conditions were used to model the inlet of the bypass and core ducts, Fig. 3a, with the values of total pressure and total temperature set based on the engine cycle. For RANS calculations a turbulence intensity of 5% and turbulence viscosity ratio of 1 was applied at the bypass and core inlets. Freestream turbulence was controlled by specifying a turbulent viscosity ratio of 1 and a turbulent intensity of 0.1%. All wall surfaces were modelled as adiabatic and viscous no-slip walls for viscous calculations.

For all installed RANS configurations a fully structured multi-block approach was used, with the resultant mesh designed for full boundary layer resolution with a $y^+ < 1$. The blocking strategy and meshing guidelines for the aircraft, engine intake, engine nacelle and exhaust nozzles were based on those outlined, and validated against experimental data, by Stańkowski et al. [41], Robinson [43] and Otter [14]. A total of three mesh resolutions were investigated such that grid independence could be assessed through the calculation of a Grid Convergence Index (GCI) [44,45]. The first cell height remained fixed across all the meshes investigated. The element count for the coarse, medium and fine meshes was 13.1, 24.0 and 43.0 million respectively. Between the medium and the fine meshes the GCI for NPF_c^D was found to be 0.1% which is within the asymptotic range. All of the computations presented within this work are based on the mesh sizing from the fine mesh (43.0 million elements). For reference, further mesh and domain inde-

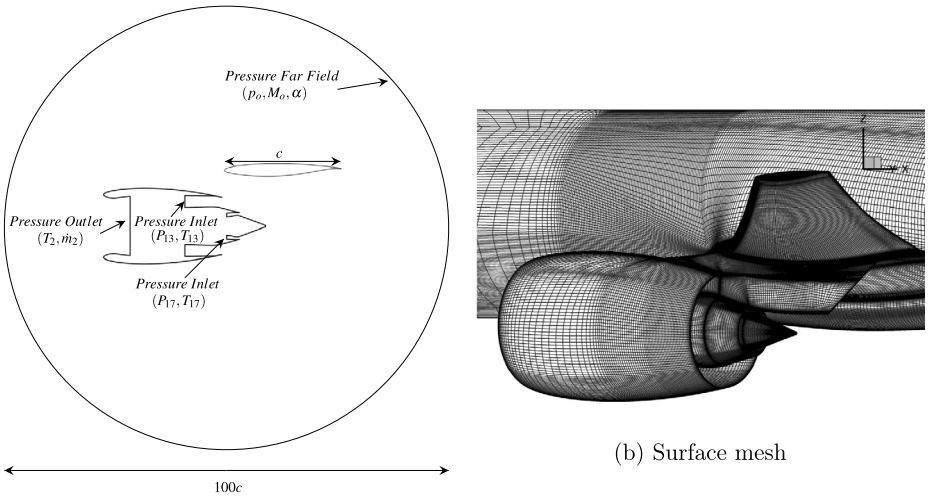

(a) Computation domain and boundary conditions

(b) Surface mesh

Fig. 3. Surface mesh and computational domain.

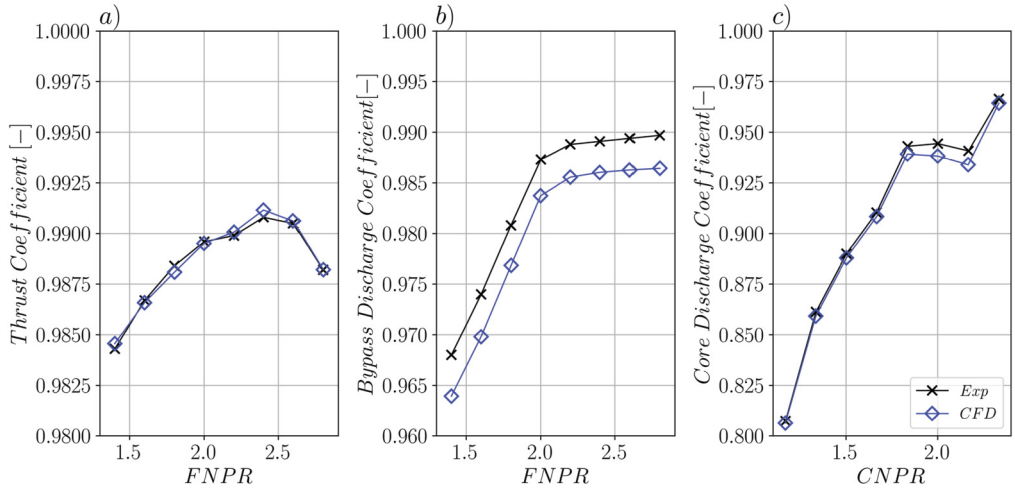

Fig. 4. Comparison between the experimental [47] and computational [14] nozzle performance of the DSFRN model.

pendence studies for the isolated and installed configurations are reported by Stańkowski [5].

3. Results and discussion

3.1. Validation of computational approach

In order to assess the validity of the computational approach, various experimental configurations were modelled. In terms of aircraft and nacelle performance, the method was found to agree with experimentally derived drag measurements to within 5% [41] and 4% [46] respectively. In addition, the change in drag due to the installation of a through-flow nacelle was calculated to within one drag count of experimental data [41]. As the major focus of this paper is on the exhaust system, a more detailed overview of this validation activity is reported hereafter with full details reported by Otter et al. [14].

The Dual Separate Flow Reference Nozzle (DSFRN) was chosen as an appropriate validation case as the experimental test data is publicly available and it was designed to be representative of a modern commercial separate-jet nozzle configuration with a by-pass ratio in the order of 10 to 12 [47]. The model consisted of two flow streams: one to simulate the flow from a fan stream and one to simulate the flow from the core engine. From the experimental testing, measurements of the thrust coefficient, bypass nozzle discharge coefficient and core nozzle discharge coefficient were taken over a range of operating points. A computational mesh of the DFRSN was generated based on the same mesh refinement guidelines that were used for the full aircraft configuration in this present study. A comparison between the experimental and computed nozzle performance metrics across multiple operating points is shown in Fig. 4. Based on a root mean squared difference between the computational and experimental data, the nozzle thrust coefficient, core and bypass coefficient were within 0.1%, 0.4% and 0.3% of experimental data respectively [14].

3.2. Exhaust design and system performance

The aim of this research was to investigate if the introduction of three-dimensional exhaust system designs would have a significant impact on the performance of the combined engine-airframe system. It is important to be able to quantify any changes to overall

Table 1
Summary of variables for DOE A design space.

Variable	Values
ψ_0	0^o, 45^o, 90^o, 135^o, 180^o, 225^o, 270^o and 315^o
$\Delta\psi$	60^o, 120^o and 180^o
$r^{out}_{BP-exit}$	0.95 and 1.05

Table 2
Design Space Bounds for DOE B.

Variable	Minimum	Maximum
$r^{in}_{BP-exit}\|_{0^o}$	0.9	1.1
$r^{in}_{BP-exit}\|_{180^o}$	0.9	1.1
β_{cc}	$\beta_{cc}\|_{ref}$	$\beta_{cc}\|_{ref} + 8^o$

system performance that result from these exhaust system designs as such designs could potentially incur penalties in other parts of the entire aircraft systems due to increased manufacturing complexity. The design study has been split into two studies: non-axisymmetric bypass nozzles (DOE A) and non-concentric bypass and core nozzles (DOE B).

3.2.1. Non-axisymmetric bypass nozzle design: DOE A

The bypass nozzle was made non-axisymmetric through the variation of $r^{out}_{BP-exit}$ (defined in Fig. 2) at various azimuthal locations. Within this design space the azimuthal variation of radius is defined by a total of three variables (Fig. 5):

- $r^{out}_{BP-exit}$, the peak or trough of the bypass exit outer radius relative to a reference value. This parameter will also be referred to as the radius ratio.
- ψ_0, the azimuthal angle at which the peak or trough in radius ratio occurs;
- $\Delta\psi$, the width (or azimuthal extent) of the radius ratio variation; note that this azimuthal extent covers the range of values for which the radius ratio does not equal 1.

As was reported by Otter et al. [19], there are two possible methods of afterbody design which could have been used to ensure that the desired nozzle exit area requirements were met. Within this investigation, a circular afterbody design method was used in order to minimise the effect that changes to the bypass nozzle had on the core nozzle. It should be further emphasised that the bypass and core nozzle geometric throat areas remained fixed for all of the designs considered within this Design of Experiments (DOE). A set of example geometries are shown in Fig. 5. A full factorial DOE approach of 48 experiments was used to explore this design space (Table 1).

The iCST distribution used to control $r^{out}_{BP-exit}$ was split into two distributions: one distribution has no variation of radius with azimuthal angle and the second with azimuthal variation of radius (Fig. 5). The first and second derivatives, $\frac{dr^{out}_{BP-exit}}{d\psi}$ and $\frac{d^2r^{out}_{BP-exit}}{d\psi^2}$ were set to be zero at the start of the uniform section (at $\psi = \psi_0 \pm \Delta\psi/2$). The gradient at the peak radius value was set to be zero, $\frac{dr^{out}_{BP-exit}}{d\psi}(\psi_0) = 0.0$.

3.2.2. Non-concentric bypass nozzle: DOE B

For the investigation of non-concentric bypass nozzles, DOE B, the inner bypass nozzle radius ($r^{in}_{BP-Exit}$) was varied azimuthally. Two azimuthal control points were used to prescribe the circumferential variation of $r^{in}_{BP-Exit}$ (Fig. 2). The first control point was at $\psi = 0^o$ and the second was at $\psi = 180^o$. Fig. 6 shows two example circumferential distributions of $r^{in}_{BP-Exit}$ in addition to polar plots for the two distributions. Within this design space the value of $r^{out}_{BP-exit}$ remained fixed throughout. A total of three variables were used to control the designs of DOE B:

- $r^{in}_{BP-Exit}(\psi = 0^o)$, the inner radius of the bypass nozzle exit at $\psi = 0^o$;
- $r^{in}_{BP-Exit}(\psi = 180^o)$, the inner radius of the bypass nozzle exit at $\psi = 180^o$;
- β_{cc}, the core cowl boattail angle for all azimuthal aerolines.

The variation of $r^{in}_{BP-Exit}$ was defined relative to the value of the axisymmetric baseline engine and took values between 0.9 and 1.1 (Table 2). Furthermore, $\frac{dr^{in}_{BP-Exit}}{d\psi}$ was specified to be zero at both $\psi = 0^o$ and $\psi = \Psi^o$ with $\frac{d^2r^{in}_{BP-Exit}}{d\psi^2}$ set to zero at $\psi = 0^o$. Moreover, the third variable (β_{cc} defined by Goulos et al. [4]) took values between $\beta_{cc}|_{ref}$ and $\beta_{cc}|_{ref} + 8^o$. Figs. 6a and 6c demonstrate two examples with a positive and negative offset of the bypass exit centre respectively. Within DOE B a total of 125 configurations were investigated with a latin hypercube sampling approach.

The core exit inner radius ($r^{in}_{CR-Exit}$) was set such that the cycle core nozzle throat area requirement was met. Similarly, the azimuthal distribution of $r^{in}_{BP-Exit}$ was scaled to met the bypass nozzle throat area requirement. The values of $r^{out}_{BP-exit}$, l_{cc} and r^{te}_{plug} (Fig. 2) were held constant, and, as a result, β_{cp} took on a circumferential variation in order to ensure that the desired value of r^{te}_{plug} was met. An example geometry is shown in the $\hat{\mathbf{e}}_\psi$-$\hat{\mathbf{e}}_r$ and $\hat{\mathbf{e}}_x$-$\hat{\mathbf{e}}_r$ planes are shown in Fig. 6. Note that the exit of the low pressure turbine (and hence the core duct inlet) remained fixed for all of the designs.

3.2.3. Selected geometries

A key consideration for exploring the design space of three-dimensional exhaust systems is the dimensionality and scope of the problem. For example, the evaluation of the potential benefits of a non-axisymmetric exhaust depends on the aerodynamic interaction with the aircraft wing and fuselage. Consequently, computational simulations require relatively large models which include both the engine and airframe. The aerodynamic interactions between the exhaust, engine and airframe comprise both inviscid and viscous elements. As the key metric is the NVF_D of the combined engine/airframe configuration, then the impact on both the lift and drag elements are of interest. This is exacerbated by the number of degrees of freedom in the geometric definition of a non-axisymmetric exhaust. Within this context, it was of interest to explore the viability of an appropriate computational strategy that would combine the refined identification of useful designs along with an increase in modelling fidelity through multiple selection steps. A two-stage filtering process was used to choose the designs which should be evaluated as full engine-airframe-pylon configurations with RANS CFD (full details of which are reported in [48]). The first step in this process was to evaluate the performance of all the designs in DOEs A and B without a pylon using an inviscid solver and a coarse unstructured mesh. These calculations provided an initial estimate for the net vehicle force based on inviscid loss mechanisms such as induced drag and shock losses. From these calculations the designs were ranked based on their net vehicle force and 15 designs were chosen. The next stage was to evaluate the chosen 15 designs with RANS CFD but without an engine pylon. Finally, 6 designs were chosen to be investigated with RANS CFD and an engine pylon: 5 from DOE A and 1 from DOE B. These cases are summarised in Table 3 and shown in Fig. 7. The six cases presented in Table 3 and Fig. 7 were chosen based on their performance when evaluated without a pylon using viscous simulations. Cases A1, A3, A4 and B1 were chosen as they were found to increase net vehicle force relative to the axisymmetric baseline. Similarly, Case A2 was investigated as this configuration

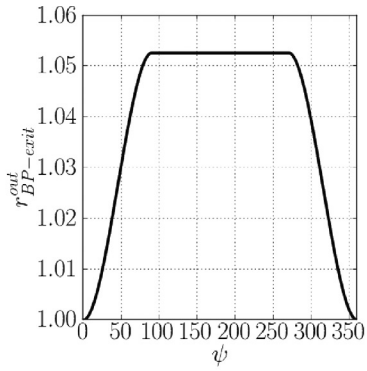

(a) Variation of $r^{out}_{BP-exit}$ for a Radius Ratio of 0.95.

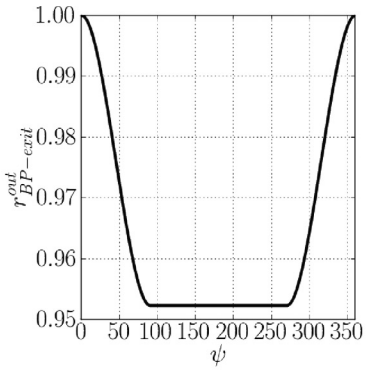

(b) Variation of $r^{out}_{BP-exit}$ for a Radius Ratio of 1.05.

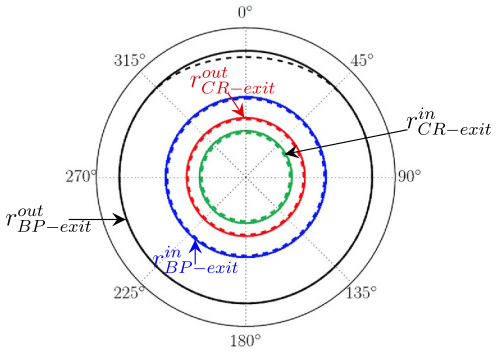

(c) Polar Plot for a Radius Ratio of 0.95. Dotted line indicates non-axisymmetric engine and solid denotes the axisymmetric reference case.

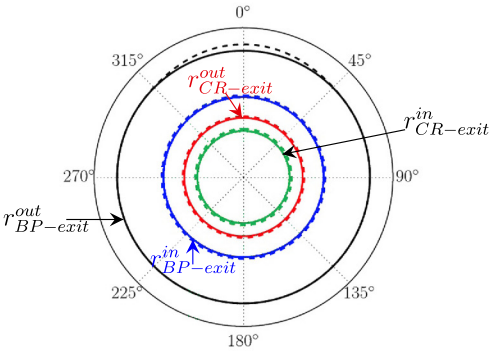

(d) Polar Plot for a Radius Ratio of 1.05. Dotted line indicates non-axisymmetric engine and solid denotes the axisymmetric reference case.

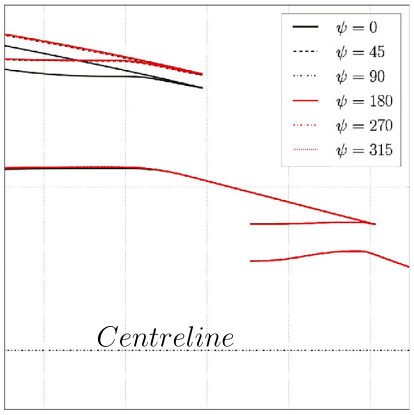

(e) $\hat{\mathbf{e}}_x$-$\hat{\mathbf{e}}_r$ Plot for a Radius Ratio of 0.95. Only the non-axisymmetric geometry is shown.

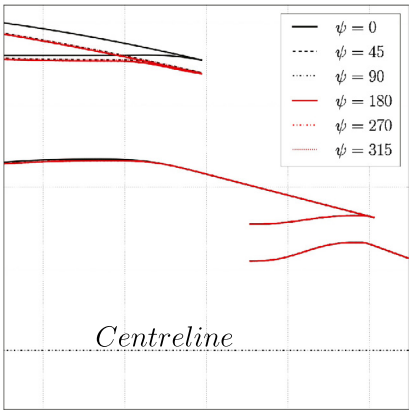

(f) $\hat{\mathbf{e}}_x$-$\hat{\mathbf{e}}_r$ Plot for a Radius Ratio of 1.05. Only the non-axisymmetric geometry is shown.

Fig. 5. DOE A design space definition and example geometries.

was found to reduce airframe drag. In terms of geometry, Cases A1 and A2 are similar as they both feature radius variation centred at the bottom line ($\psi = 180^o$) of the exhaust system, as shown in Figs. 7a and b. Cases A3 and A4 both feature a reduction of radius at the inboard and outboard sidelines ($\psi = 90^o$ and $\psi = 270^o$) of the exhaust systems, Figs. 7c and d. Case A5 (Fig. 7e) features an increased ground clearance, equal to 5% of the nacelle trailing edge radius, compared to the axisymmetric baseline case. This is achieved as the topline radius has been reduced by 5% and the entire engine has been translated to keep the same vertical offset between the wing leading edge and nacelle trailing edge. Case B1 features a non-concentric bypass nozzle with the inner annulus of the bypass nozzle offset away from the aircraft wing (Fig. 7f). The variation of the aerodynamic performance metrics for the six designs is presented in Section 3.2.4, with the associated flow physics analysed in Section 3.3.

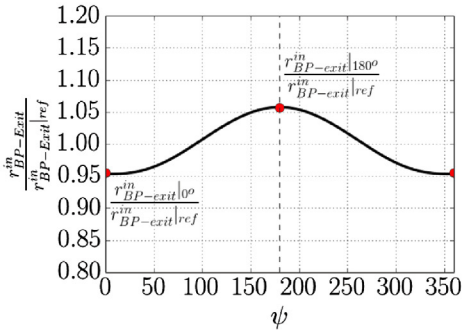

(a) Example 1 distribution of $r^{in}_{BP-exit}$

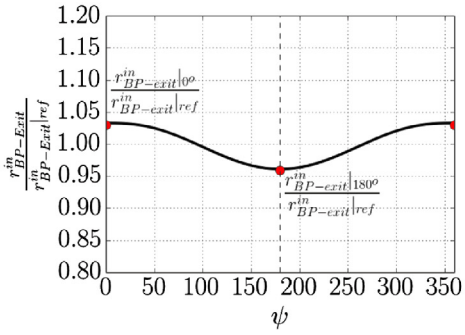

(b) Example 2 distribution of $r^{in}_{BP-exit}$

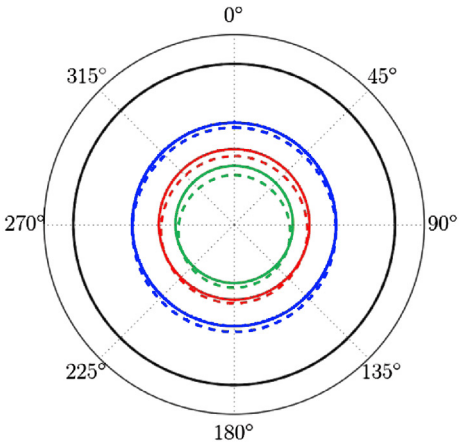

(c) Example 1 polar plot.Dotted line indicates non-axisymmetric engine and solid denotes the axisymmetric reference case.

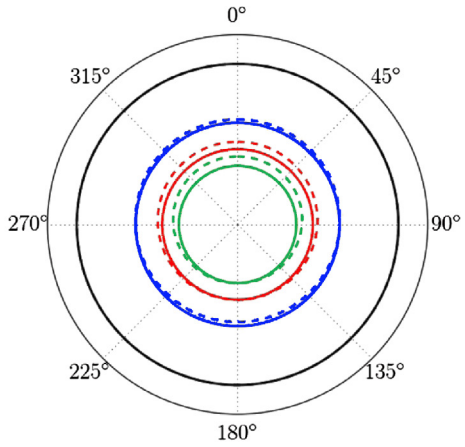

(d) Example 2 polar plot.Dotted line indicates non-axisymmetric engine and solid denotes the axisymmetric reference case.

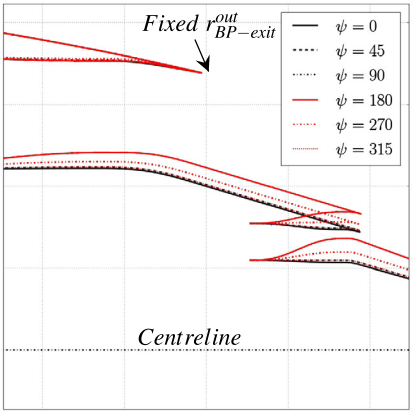

(e) Example 1 $\hat{\mathbf{e}}_x$-$\hat{\mathbf{e}}_r$ plane plot.

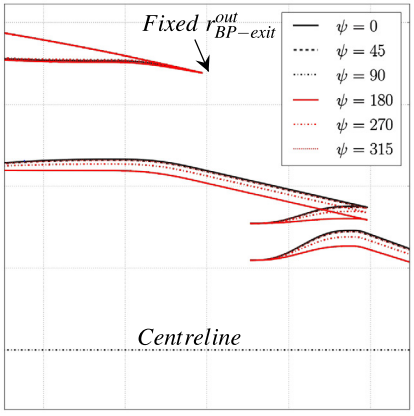

(f) Example 2 $\hat{\mathbf{e}}_x$-$\hat{\mathbf{e}}_r$ plane plot.

Fig. 6. DOE B design space definition and example geometries.

3.2.4. Aerodynamic performance

As each engine design altered the airframe wing loading, an incidence sweep was calculated from 2^o to 3^o in order to ensure that net vehicle force could be evaluated at an aircraft lift coefficient of 0.5. The change in cruise incidence was found to be small and varied between 2.3^o and 2.4^o for the cases considered. From the six cases which were investigated, two cases have an increased net vehicle force compared to the axisymmetric baseline case (Table 4). Those were Case A1 (reduced nacelle trailing edge radius on the bottomline, Fig. 7a) and Case B1 (non-concentric bypass exit which is offset away from the wing, Fig. 7b) with changes in net vehicle force equal to 0.8% and 0.6% respectively. Given the

Table 3
Summary of design parameters.

Case	ψ_0	$\Delta\psi$	$r^{out}_{BP-exit}\|_\psi$	Rationale
A1	180^o	180^o	0.95	High NVF without pylon
A2	180^o	180^o	1.05	Low airframe drag without pylon
A3	270^o	60^o	0.95	High NVF without pylon
A4	90^o	60^o	0.95	High NVF without pylon
A5	0^o	120^o	0.95	Increased ground clearance
Case	$r^{in}_{BP-exit}(0^o)$	$r^{in}_{BP-exit}(180^o)$	$\beta_{cc} - \beta^{axi}_{cc}$	
B1	0.95	1.06	3.1	High NVF without pylon

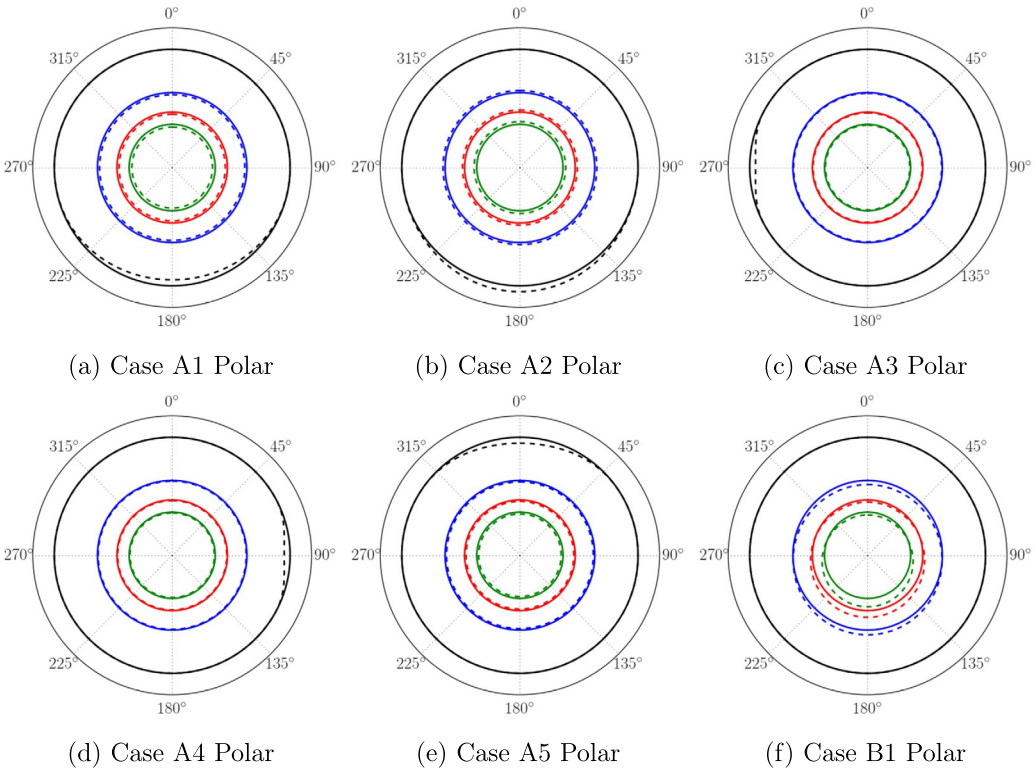

(a) Case A1 Polar (b) Case A2 Polar (c) Case A3 Polar

(d) Case A4 Polar (e) Case A5 Polar (f) Case B1 Polar

Fig. 7. Summary of Non-axisymmetric Bypass Nozzles. Dotted line indicates non-axisymmetric engine and solid denotes the axisymmetric reference case.

Table 4
Summary of net vehicle force variations.

Case	ΔNVF^D (%)
A1	0.8
A2	-3.0
A3	-0.2
A4	-0.1
A5	-0.6
B1	0.6

higher value of net vehicle force for Case A1, this suggests that the reduction of nacelle trailing edge radius at the bottom line of the engine is a promising design option for closely-coupled high-bypass ratio aero-engines. The increase in net vehicle force for both Cases A1 and B1 demonstrates that non-axisymmetric bypass nozzles can produce aerodynamic benefits for the combined engine-airframe system. Not only are net vehicle thrust increases significant in terms of potential fuel burn reduction, they also provide the possibility to locate the engine in a position with mechanical or operational benefits. Therefore, it can be concluded that non-axisymmetric bypass nozzles represent an enabling technology for the installation of future turbofan engines.

Through the inspection of the aerodynamic performance breakdown (Fig. 8a), the beneficial net vehicle force for Cases A1 and B1 can be seen to result from an increased NPF^D_c relative to the axisymmetric case. In both cases this increase to net propulsive force results from a combination of increased gross propulsive force and a reduction in modified nacelle drag. As the corrected gross propulsive force is evaluated with constant corrected nozzle mass flow rates it can be concluded that the increased value of gross propulsive force results from a more efficient nozzle design rather than an increased nozzle mass flow rate. Both cases feature an increased airframe drag relative to the axisymmetric case, which serves to reduce the benefit of the increased net propulsive force.

For Case A2 (Fig. 7b), which was considered due to the reduced airframe drag when computed without a pylon, there is a net vehicle force penalty of 3% (Fig. 8a and Table 4). The majority of this penalty results from a reduction to NPF^D_c due to a loss of GPF^D_{c*} and increase to modified nacelle drag. However, Case A2 displays a reduction in airframe drag but this is not enough to outweigh the penalising reduction in net propulsive force. This serves as evidence that increases to the bypass nozzle trailing edge radius at

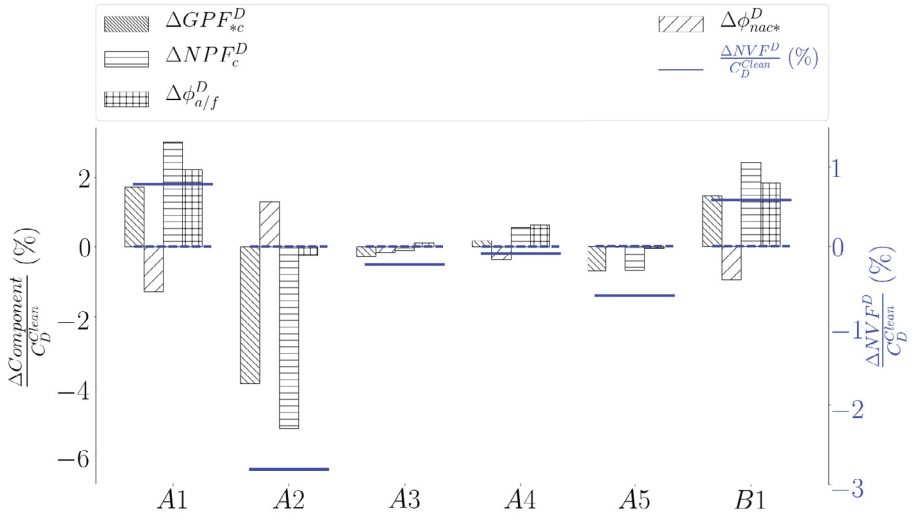

(a) Aerodynamic performance

Fig. 8. Summary of aerodynamic performance.

the bottomline of the annulus should be avoided, as it presents no mechanical or aerodynamic benefits.

Cases A3 and A4 (Figs. 7c and d), where the exhaust geometry was modified at 270^o and 90^o respectively, report a reduction in net vehicle force with values of -0.2% and -0.1% respectively (Fig. 8a and Table 4). With a reduction of bypass trailing edge radius on the inboard side, Case A3 shows a beneficial reduction in nacelle drag but with a concurrent reduction to gross propulsive force and increase to airframe drag. Case A4 remains neutral in terms of modified nacelle drag and is insensitive to airframe drag, the excess thrust penalty of -0.08% is primarily due to a reduction in gross propulsive force. Although these particular cases do not show an improvement over the axisymmetric baseline engine, there may be scope for improvements if the airframe geometry were to be altered in tandem with the exhaust nozzle in an effort to reduce $\phi^D_{a/f}$. Finally, case A5 (reduced topline nacelle trailing edge radius, Fig. 7e), demonstrates that an increase in ground clearance by 5% of the nacelle trailing edge radius results in a net vehicle force reduction of 0.6%.

3.3. Flow physics

From the aerodynamic performance analysis, it was demonstrated that Case A1 showed a reduction in nacelle drag compared to the axisymmetric baseline configuration and conversely Case A2 showed an increase to modified nacelle drag. The cause for the change to modified nacelle drag lies in the static pressure over the nacelle afterbody (Fig. 9). Between the axisymmetric baseline, Case A1 and Case A2, the viscous forces remained constant and hence any changes in the overall force were a result of variations to the static pressure. Over the afterbody of the nacelle there is a higher pressure coefficient for Case A1 relative to Case A2 (Fig. 9). When integrated over the entire nacelle afterbody, this increase in static pressure leads to the reduction of modified nacelle drag for Case A1 and conversely the reduction in static pressure leads to an increase of modified nacelle drag for Case A2. A similar mechanism of nacelle drag reduction was observed during the engine-only bypass nozzle design space exploration of Otter et al. [19].

In terms of airframe drag the major difference between cases A1 and A2 can be observed on the forward part of the wing pressure surface (Figs. 9, 10a and 10d). In a similar vein to the above method for modified nacelle drag reduction, the variation arises due to changes in static pressure. At a position inboard of the engine the minimum static pressure around the forebody of the wing is lower for Case A2 compared to that at across the same position for Case A1. Due to the forward facing projected area of this portion of the wing forebody a lower static pressure results in a reduction in airframe drag for Case A2 compared to Case A1. Between Cases A1 and A2 the shock on the lower surface of the wing changes strength and axial location (Fig. 10). In terms of the pylon, the variation in static pressure is much more pronounced on the inboard side compared to the outboard (Fig. 10). Case A2 is subject to a larger acceleration, and hence lower pressure, across the entire span of the pylon's inboard side compared to Case A1 (Figs. 10b and 10e). It is the shock wave and acceleration on the inboard side of the pylon which has the largest influence on the performance of the exhaust system.

For all three configurations a normal shock wave is present between the airframe wing and inboard side of the pylon (as shown in Fig. 11). This shock arises due to the formation of a supersonic region in the gully between the engine and the airframe. The strength of this shock wave is altered as the exhaust nozzle design is changed, with the exhaust nozzle of Case A1 reducing the strength of this shock and Case A2 serving to increase the strength (Figs. 11a and 11c). In addition to the shock wave itself there is also a low pressure region on the core cowl upstream of the shock which leads to a loss of thrust. In a similar manner to the nacelle afterbody, a reduction in pressure on the exhaust afterbodies results in a drag; or due to the location of the exhaust afterbody in the engine streamtube, a loss of thrust. Therefore, designs should aim to increase the static pressure on the afterbody. Case A2 has a reduction in gross propulsive force compared to the axisymmetric case due to this increased acceleration on the exhaust core cowl (Fig. 11c). Conversely Case A1 shows an increase to gross propulsive force as the static pressure is increased on the exhaust afterbody (Fig. 11a). The cause of this change between the two cases arises due to the change in the wing-engine gully size.

No detailed aerodynamic analysis is presented for Cases A3 to A5 as the major mechanisms for modified nacelle drag and aircraft drag reductions are the same as those reported for Cases A1 to A2. That is variations in static pressure around the nacelle afterbody and wing forebody. However, due to the beneficial net vehicle force, the flow physics of case B1 are presented below.

From a flow physics perspective, the major cause for the increase to modified gross propulsive force for case B1 is due to the

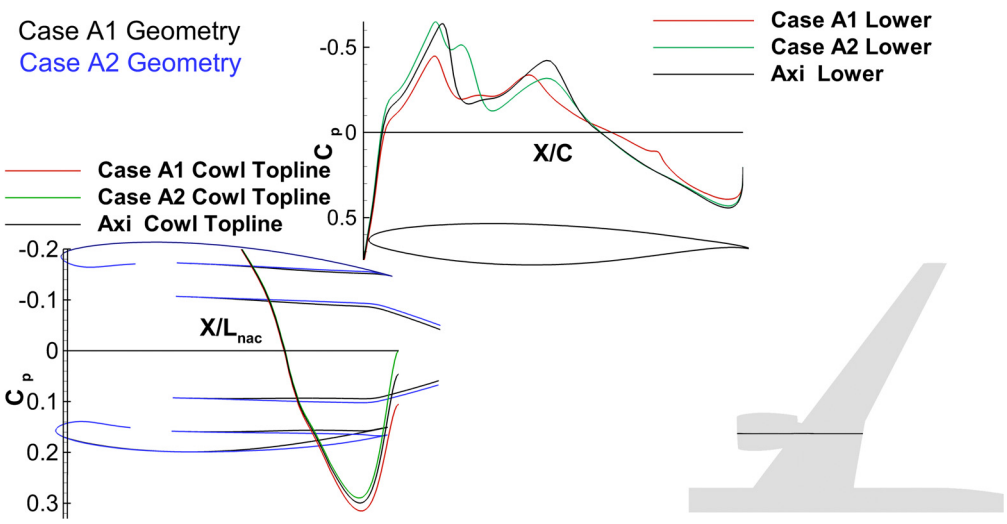

Fig. 9. Variation of static pressure for Cases A1 and A2. At $M_0 = 0.85$ at $\alpha = 2.0$ for an axial cut inboard of the engine pylon. Note that for clarity the core nozzle or axisymmetric geometry is not shown.

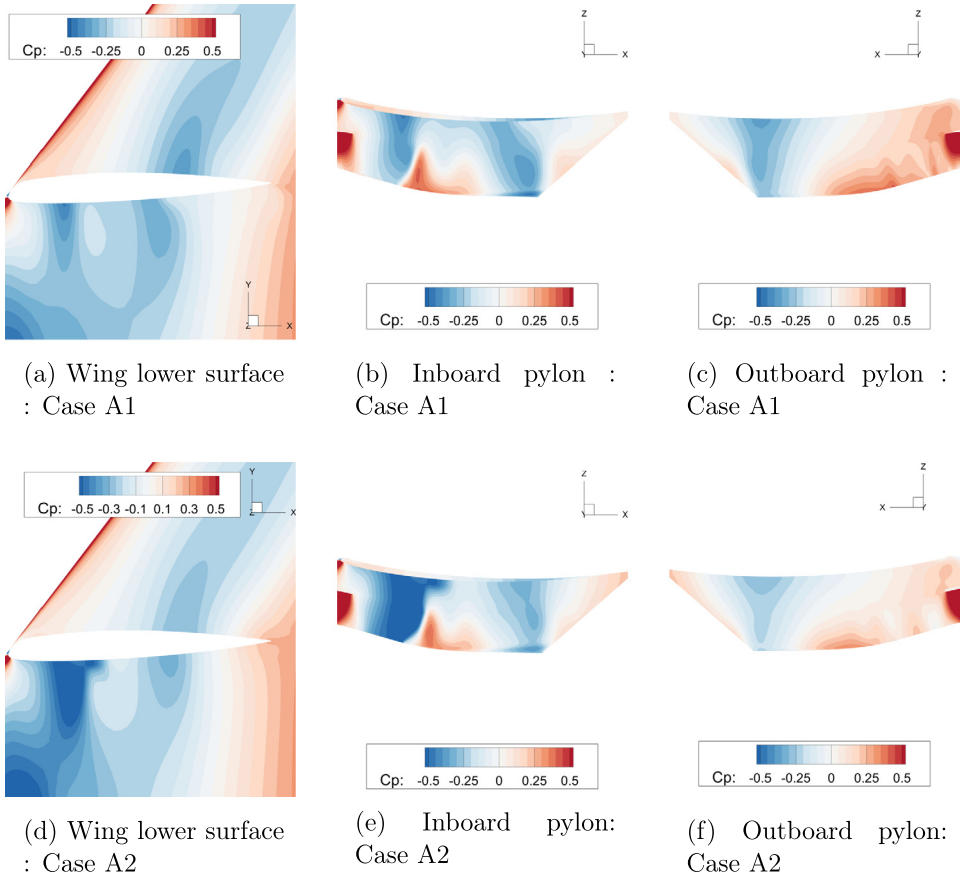

(a) Wing lower surface : Case A1

(b) Inboard pylon : Case A1

(c) Outboard pylon : Case A1

(d) Wing lower surface : Case A2

(e) Inboard pylon: Case A2

(f) Outboard pylon: Case A2

Fig. 10. Distribution of static pressure for Case A1 and Case A2 at $\alpha = 2.0$ and $M_0 = 0.85$.

reduced strength of the shock on the inboard side of the core cowl. This is demonstrated by the lower pre-shock static pressure on the engine pylon and core cowl for Case B1 compared to the axisymmetric case (Figs. 12a and 12b). In addition to the shock strength, this design also increases the average static pressure on the exhaust afterbody which in turn provides an increase on the thrust generated on this body. As was demonstrated in the previous section, the change in modified nacelle drag arises due variations in static pressure on the nacelle afterbody. However, in the case of B1 there is no change in the nacelle geometry between B1 and the axisymmetric case. Therefore this change in modified nacelle drag arises due to the non-uniform flow at the exit of the bypass nozzle which subsequently alters the shape and curvature of the engine's post-exit streamtube.

4. Conclusions

Within this paper a design approach for installed non-axisymmetric aero-engine exhaust systems has been developed. An aerodynamic assessment of six engine-airframe configurations

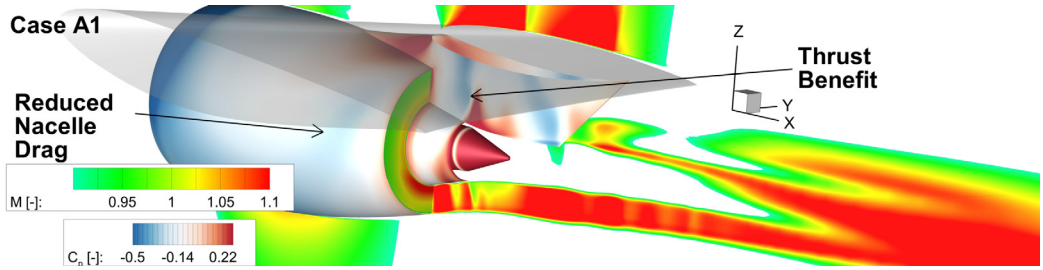

(a) Case A1

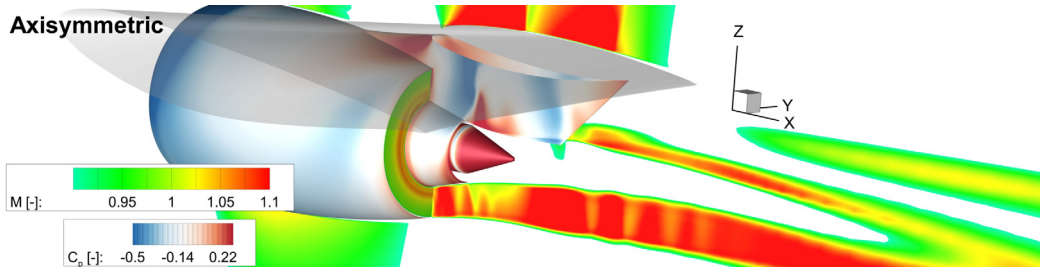

(b) Axisymmetric

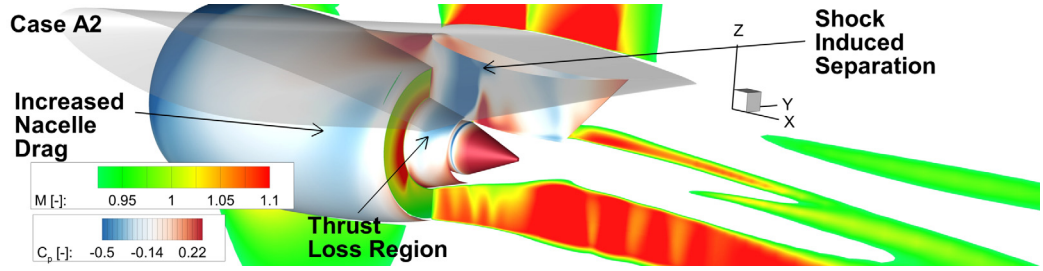

(c) Case A2

Fig. 11. Distribution of Mach number (through the $\hat{\mathbf{e}}_x$-$\hat{\mathbf{e}}_z$ plane) and static pressure (on each surface) for three configurations at $\alpha = 2.0$ and $M_0 = 0.85$.

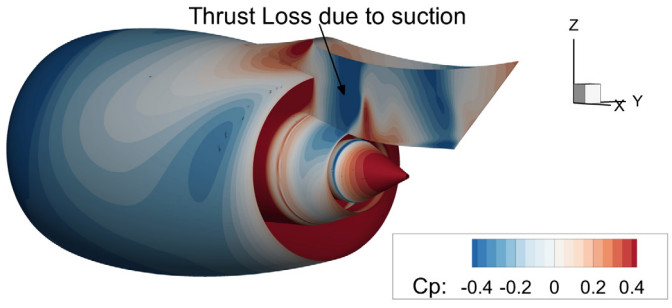

(a) Axisymmetric

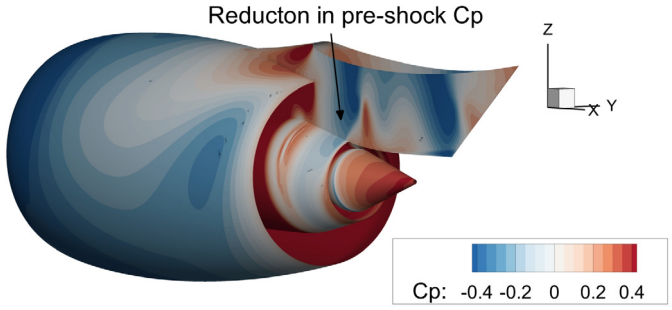

(b) Case B1

Fig. 12. Distribution of static pressure for the axisymmetric baseline and Case B1 engine at $\alpha = 2.0$ and $M_0 = 0.85$.

has been undertaken using computational fluid dynamics. Two design space exploration activities have been presented, the first was based on the introduction of azimuthal variations to the bypass nozzle outer radius ($r^{out}_{BP-exit}$). The second investigated circumferential variations to the bypass inner nozzle radius ($r^{in}_{BP-exit}$) and the core nozzle outer radius ($r^{out}_{CR-exit}$).

The most eminent non-axisymmetric bypass nozzle and exhaust afterbody designs were found to increase net vehicle force by 0.8% and 0.6% respectively. The best design from the bypass nozzle investigation featured a reduction to the bypass nozzle outer radius at an azimuthal angle of 180 degrees. The most notable design from the afterbody DSE featured a variation of $r^{in}_{BP-exit}$ such that the bypass inner annulus was offset in the radial direction relative to the outer annulus. Therefore, non-axisymmetric exhaust system designs have demonstrated the capability to reduce the aerodynamic penalties associated with closely-coupled installation positions at cruise conditions.

For both sets of non-axisymmetric exhaust system designs, a reduction of modified nacelle drag was the primary reason for the increased values of excess thrust. The aerodynamic mechanism responsible arose due to the reduction of accelerations over the afterbody of the nacelle. In addition, non-axisymmetric designs were found to increase the efficiency of the exhaust system by reducing the strength of the shock wave which formed between the wing and inboard side of the engine pylon. This demonstrates the potential benefits of novel exhaust designs as well as highlighting the necessity to analyse design changes to the aero-engine exhausts and nacelle as part of engine-airframe system.

Now that non-axisymmetric exhaust system designs have been shown to exhibit aerodynamic benefits relative to axisymmetric designs there are number of avenues which should be investigated to ensure that such designs can fulfil their potential at a system level. As this study has only considered mid-cruise conditions the effect of non-axisymmetric exhaust system designs at other conditions such as take-off should be considered. Moreover, as the airframe geometry remained fixed in this investigation, the notion of a joint engine-airframe optimisation study could be undertaken in order to maximise potential performance benefits. Finally, a mission level analysis of fuel burn savings between the sets of designs should be undertaken so that potential issues such as increased mechanical complexity and hence the weight of non-axisymmetric engines could be evaluated.

Declaration of competing interest

The authors declare that they have no known competing financial interests or personal relationships that could have appeared to influence the work reported in this paper.

Acknowledgements

The doctoral studies of John Otter were funded by Rolls-Royce plc. and the Engineering and Physical Science Research Council (Industrial Case Award 14220163). Due to commercial confidentiality agreements the supporting data is not available. The authors would like to thank J. C. Vassberg for making the geometry of the Common Research Model available.

References

[1] N.T. Birch, 2020 vision: the prospects for large civil aircraft propulsion, Aeronaut. J. 104 (1038) (2000) 347–352.
[2] A. Guha, Optimum fan pressure ratio for bypass engines with separate or mixed exhaust streams, J. Propuls. Power 17 (5) (2001) 1117–1122.
[3] J. Zhang, Z. Zhou, W. Wei, Y. Deng, Aerodynamic design of an ultra-low rotating speed geared fan, Aerosp. Sci. Technol. 63 (2017) 73–81.
[4] I. Goulos, T. Stankowski, J. Otter, D. MacManus, N. Grech, C. Sheaf, Aerodynamic design of separate-jet exhausts for future civil aero-engines part I: parametric geometry definition and computational fluid dynamics approach, J. Eng. Gas Turbines Power 138 (8 (GTP-15-1538)) (2016), https://doi.org/10.1115/1.4032649.
[5] T.P. Stankowski, D.G. MacManus, M. Robinson, C.T. Sheaf, Aerodynamic effects of propulsion integration for high bypass ratio engines, J. Aircr. 54 (6) (2017), https://doi.org/10.2514/1.C034150.
[6] T. Sibilli, M. Savil, V. Sethi, D. MacManus, A. Rolt, Numerical simulation of propulsion systems integration for very high bypass ratio engines, in: Proceedings of ASME Turbo Expo GT2012, no. GT2012-68908, 2012.
[7] T. Sibilli, Modelling the aerodynamics of propulsive system integration at cruise and high-lift conditions, Ph.D. thesis, Department of Power and Propulsion, Cranfield University, 2012.
[8] J.D. Mattingly, Elements of Gas Turbine Propulsion, McGraw-Hill, 2006.
[9] J.R. DeBonis, Gas turbine engines: nozzles, in: Encyclopedia of Aerospace Engineering, 2010, pp. 1–11.
[10] I. Goulos, J. Otter, T. Stankowski, D. MacManus, N. Grech, C. Sheaf, Aerodynamic design of separate-jet exhausts for future civil aero-engines part II: design space exploration, surrogate modeling, and optimization, J. Eng. Gas Turbines Power 138 (8) (2016).
[11] I. Goulos, T. Stankowski, D. MacManus, P. Woodrow, C. Sheaf, Civil turbofan engine exhaust aerodynamic: impact of bypass nozzle after-body design, Aerosp. Sci. Technol. 73 (2018).
[12] I. Goulos, D. MacMacnus, C. Sheaf, Civil turbofan engine exhaust aerodynamics: impact of fan exit flow characteristics, Aerosp. Sci. Technol. 93 (2019).
[13] G. Giangaspero, D. MacManus, I. Goulos, Surrogate models for the prediction of the aerodynamic performance of exhaust systems, Aerosp. Sci. Technol. 92 (2019) 77–90.
[14] J. Otter, I. Goulos, D. MacManus, M. Slaby, Aerodynamic analysis of civil aero-engine exhaust systems using computational fluid dynamics, J. Propuls. Power 34 (5) (2018) 1152–1165.
[15] R.H. Thomas, K.W. Kinzie, Jet-pylon interaction of high bypass ratio separate flow nozzle configurations, in: 10th AIAA/CEAS Aeroacoustics Conference, no. AIAA Paper 2004-2827, Manchester, UK, 2004.
[16] D. Munday, M. Mihaescu, E. Gutmark, Experimental and numerical study of jets from elliptic nozzles with conic plug, AIAA J. 49 (3) (2011) 554–564, https://doi.org/10.2514/1.J050587.
[17] R.H. Thomas, Y. Guo, J.J. Berton, H. Fernandez, Aircraft noise reduction technology roadmap toward achieving the nasa 2035 noise goal, in: AIAA SciTech Forum, 55th AIAA Aerospace Sciences Meeting, no. AIAA Paper 2017-3193, 2017.
[18] J.J. Otter, T. Stankowski, M. Robinson, D. MacManus, Installation aerodynamics of civil aero-engine exhaust systems, Aerosp. Sci. Technol. 89 (2019) 345–355.
[19] J.J. Otter, R. Christie, I. Goulos, D. MacManus, N. Grech, Parametric design of non-axisymmetric separate-jet aero-engine exhaust systems, Aerosp. Sci. Technol. 93 (2019).
[20] D.L. Berry, The boeing 777 engine/aircraft integration aerodynamic design process, ICAS-Paper no. 94-6.4.4, 1994.
[21] L. Wiart, O. Atinault, B. Paluch, D. Hue, R. Grenon, Development of nova aircraft configurations for large engine integration studies, in: AIAA Aviation June 2015 Dallas 33rd AIAA Applied Aerodynamics Conference, no. AIAA 2015-2254.
[22] H. Hoheisel, Aerodynamic aspects of engine-aircraft integration of transport aircraft, Aerosp. Sci. Technol. 7 (1997) 475–487.
[23] A. Heidebrecht, D. MacManus, Surrogate model of complex non-linear data for preliminary nacelle design, Aerosp. Sci. Technol. 84 (2019).
[24] F. Tejero, M. Robinson, D. MacManus, C. Sheaf, Multi-objective optimisation of short nacelles for high bypass ratio engines, Aerosp. Sci. Technol. 91 (2019) 410–421.
[25] M. Robinson, D.G. MacManus, A. Heidebrecht, N. Grech, An optimization method for nacelle design, in: AIAA SciTech Forum, 55th AIAA Aerspace Sciences Meeting, no. AIAA Paper 2017-0708, 2017.
[26] M. Robinson, D.G. MacManus, K. Richards, C. Sheaf, Short and slim nacelle design for ultra-high bpr engines, in: AIAA SciTech Forum, 55th AIAA Aerospace Sciences Meeting, no. AIAA Paper 2017-0707, 2017.
[27] A.W. Chen, M.M. Curtin, R.B. Carlson, E.N. Tinoco, Tranair applications to engine/airframe integration, AIAA J. Aircr. 27 (8) (1990) 716–721.
[28] L. Jing, G. Zhenghong, H. Jiangtao, Z. Ke, Aerodynamic design optimization of nacelle/pylon position on an aircraft, Chin. J. Aeronaut. 26 (4) (2013) 850–857.
[29] T. Saitoh, H.-J. Kim, K. Takenaka, K. Nakahashi, Multi-point design of wing-body-nacelle-pylon configuration, in: 24th Applied Aerodynamics Conference, no. AIAA 2006-3461, 2006.
[30] S. Koc, H.-J. Kim, K. Nakahashi, Aerodynamic design of wing-body-nacelle-pylon configuration, in: 17th AIAA Computational Fluid Dynamics Conference, no. AIAA 2005-4856, 2005.
[31] B. Epstein, S. Peigin, Automatic optimization of wing-body-under-the-wing-mounted-nacelle configurations, J. Aircr. 53 (3) (2016) 691–700.
[32] R. Lei, J. Bai, D. Xu, Aerodynamic optimization of civil aircraft with wing-mounted engine jet based on adjoint method, Aerosp. Sci. Technol. 93 (2019).

[33] MIDAP Study Group, Guide to in-flight thrust measurement of turbojets and fan engines, Advisory Group for Aerospace Research and Development (AGARDograph No. 237), 1979.
[34] J.C. Vassberg, et al., Development of a common research model for applied cfd validation studies, in: 26th AIAA Applied Aerodynamics Conference, no. AIAA 2008-6919.
[35] Z. Zhu, N. Qin, Intuitive class/shape function parameterization for airfoils, AIAA J. 52 (1) (2014) 17–24.
[36] B.M. Kulfan, Recent extensions and applications of the 'cst' universal parametric geometry representation method, Aeronaut. J. 114 (1153) (2010) 157–176.
[37] B.M. Kulfan, Universal parametric geometry representation method, J. Aircr. 45 (1) (2008) 142–158.
[38] D. Guénot, F. Gallard, J. Brézillon, Y. Mérillac, Aerodynamic optimisation of a parametrised engine pylon on a mission path using the adjoint method, Int. J. Comput. Fluid Dyn. 33 (6–7) (2019) 289–301.
[39] J.M. Weiss, J.P. Maruszewski, W.A. Smith, Implicit solution of the Navier-Stokes equations on unstructured meshes, no. AIAA Paper 97-2103, 1997.
[40] F.R. Menter, Two-equation eddy-viscosity turbulence models for engineering applications, AIAA J. 32 (8) (1994) 1598–1605, https://doi.org/10.2514/3.12149.
[41] T.P. Stankowski, D.G. MacManus, C.T. Sheaf, R. Christie, Aerodynamics of aero-engine installation, Proc. Inst. Mech. Eng., G J. Aerosp. Eng. 230 (14) (2016).
[42] E.N. Tinoco, D. Levy, O. Brodersen, Aiaa 4th drag prediction workshop, https://aiaa-dpw.larc.nasa.gov/Workshop4/workshop4.html, 2009. (Accessed 13 April 2015), https://aiaa-dpw.larc.nasa.gov/Workshop4/.
[43] M. Robinson, Aero-engine installation effects for novel ultra-high bypass ratio configurations, Ph.D. thesis, Cranfield University, 2018.
[44] P. Roache, Perspective: a method for uniform reporting of grid refinement studies, J. Fluids Eng. 116 (3) (1994) 405–413, https://doi.org/10.1115/1.2910291.
[45] P.J. Roache, Quantification of uncertainty in computational fluid dynamics, Annu. Rev. Fluid Mech. 29 (1997) 129–160, https://doi.org/10.1146/annurev.fluid.29.1.123.
[46] M. Robinson, D.G. MacManus, C. Sheaf, Aspects of aero-engine nacelle drag, Proc. Inst. Mech. Eng., G J. Aerosp. Eng. (2018).
[47] K.L. Mikkelsen, D.J. Myren, D.G. Dahl, M.D. Christiansen, Initial subscale performance measurements of the aiaa dual separate flow reference (dsfr) nozzle, in: 51st AIAA/SAE/ASEE Joint Propulsion Conference, 2015.
[48] J.J. Otter, Aerodynamics and performance of civil aero-engine exhaust systems, Ph.D. thesis, School of Aerospace Management and Technology, Cranfield University, 2018.

2020-09-17

Design and analysis of non-axisymmetric installed aero-engine exhaust systems

Otter, John J.

Elsevier

Otter JJ, Goulos I, Christie R, MacManus DG. (2020) Design and analysis of non-axisymmetric installed aero-engine exhaust systems. Aerospace Science and Technology, Volume 106, November 2020, Article number 106210

https://doi.org/10.1016/j.ast.2020.106210